Chemistry Europe
European Chemical Societies Publishing

WILEY VCH

Excellence in Chemistry Research



Announcing our new flagship journal

- Gold Open Access
- Publishing charges waived
- Preprints welcome
- Edited by active scientists

Meet the Editors of *ChemistryEurope*



Luisa De Cola
Università degli Studi di Milano Statale, Italy



Ive Hermans
University of Wisconsin-Madison, USA



Ken Tanaka
Tokyo Institute of Technology, Japan



Synergistically Interfaced Bifunctional Transition Metal Selenides for High-Rate Hydrogen Production Via Urea Electrolysis

Bezawit Z. Desalegn,[a] Kim Hern,[a] and Jeong Gil Seo*[b]

The realization of carbon-neutral energy is regarded a prime challenge as the environment and energy have become two key issues facing modern society. Here, synergistically interfaced transition metal selenides are studied for hydrogen production via urea electrolysis with concurrent environmental treatment. Extremely low overpotentials of 210 mV, 250 mV, and 1.41 V vs. RHE were observed at 100 mA cm^{-2} for HER, OER and UOR, respectively with a 98.3% faradaic efficiency. A notably low cell voltage of 1.6 and 1.84 V was required at 200 mA cm^{-2} for urea and water electrolysis, respectively along with a remarkably stable performance for 4 days. Additionally, A 1.45-fold increase in H_2 production rate was observed for urea electrolysis [26.6 μmol min^{-1}] when compared with water electrolysis [18 μmol min^{-1}] decreasing the power consumption by 37%. Real human urine electrolysis was conducted with excellent performance requiring a cell voltage of only 1.9 V at 200 mA cm^{-2}, attributed to the synergistic intermediate-active site interaction, improved charge transfer capability, and slow surface transformation-induced activation.

Introduction

Demand for the decarbonization of energy sources and storage of surplus renewable energy in chemical bonds has accelerated the need for efficient and low-cost hydrogen production. Water electrolysis is a promising strategy for producing sustainable and carbon-neutral renewable energy.[1] However, only 4% of total hydrogen production is accounted for water electrolysis, with the main reason being system inefficiency. The electricity expenses of an industrial water electrolyzer are significantly more than the cost of the noble metal electrocatalyst required.[2] Moreover, conventional water electrolyzers produce H_2 and O_2 simultaneously, which gives rise to the danger of explosion and the degradation of cell membranes, resulting in premature device failure.[3]

Among several viable approaches being undertaken to enhance the catalytic performance of cathodic HER and anodic OER, chemical-assisted hydrogen electrocatalytic evolution (CAHER) has experienced exponential growth.[2] In this system, alternative anodic reactions with either value added, or inert products are explored aiming to provide the necessary electrons for the HER with minimal energy requirement.[2] A large amount of wastewater is produced from human and animal excreta and during the industrial synthesis of urea,[4] suggesting urea as a promising source for hydrogen production.[5]

In this regard, the use of urea-rich wastewater for hydrogen production has been the focus of interest as an alternative renewable energy source. The UOR provides more economic electrons than OER because of its lower thermodynamic barriers, which results in 36% lower cost and 30% less energy requirement.[6] Hence, urea electrolysis provides a promising channel for hydrogen generation while eliminating harmful urea in urea-rich wastewater.[1]

Under standard conditions, the theoretical thermodynamic overall cell voltage for urea electrolysis (0.37 V) is significantly lower than that of water electrolysis (1.23 V). However, 6e$^-$ transfer processes, multiple sluggish gas desorption steps, and complicated intermediate transfers have been masking the energetic advantages of UOR over OER.[7] Confirmed by the hydrolysis of urea in urease, nickel has been recognized as an effective candidate for UOR. During UOR, an active Ni^{3+} species is formed via the deprotonation of a surface hydroxide group by hydroxide present in solution, which oxidizes urea and is chemically reduced back to the inactive Ni^{2+}.[8] Therefore, an increased number of oxidized species could bring forth further improvement in the catalytic activity. However, pure phases of transition metal oxides/hydroxides pose a fatal weakness on electron transfer capability.[9] In addition, the unfavorably strong binding of Ni^{3+} active sites with *COO intermediates poses a challenge towards the long-term performance of electrodes.[10,11]

As a result, transition metal chalcogenides (TMCs) have been endorsed as efficient electroactive materials to promote HER and OER/UOR processes because of their high intrinsic electrical conductivity, abundance, and cost effectiveness.[9] Specifically, Se, being a semiconductor, possesses significantly

[a] B. Z. Desalegn, Prof. K. Hern
Department of Energy Science and Technology
Myongji University
116 Myongji-ro, Cheoin-gu, Yongin-Si, Gyeonggi-do, Republic of Korea
[b] Prof. Dr. J. Gil Seo
Department of Chemical Engineering
Hanyang University
222 Wangshimni-ro, Seongdong-gu,
Seoul 04763, Republic of Korea
E-mail: jgseo@hanyang.ac.kr

Supporting information for this article is available on the WWW under https://doi.org/10.1002/cctc.202100969

© 2021 Wiley-VCH GmbH

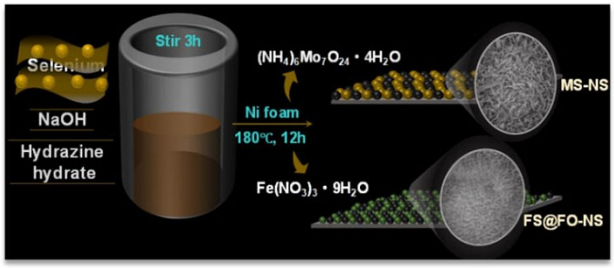
18673899, 2022, 1, Downloaded from https://chemistry-europe.onlinelibrary.wiley.com/doi/10.1002/cctc.202100969 by Hanyang University Library, Wiley Online Library on [19/02/2023]. See the Terms and Conditions (https://onlinelibrary.wiley.com/terms-and-conditions) on Wiley Online Library for rules of use; OA articles are governed by the applicable Creative Commons License

higher conductivity than O and S with similar electrochemical properties, providing faster electrochemical reaction capability.[12] Multicomponent structures of Fe, Mo, and Ni selenides have been investigated as efficient OER and HER electrocatalysts.[13–16] However, reports on TM selenides for UOR are rare.[10,17]

It is of significant importance to realize a simplified system whereby; low cost and high-performance bifunctional electrodes are utilized for both OER/UOR and HER. Thus, taking these observations and findings into consideration, the multifaceted synergistic attributes of Fe and Mo on the HER, OER, and UOR activities of nickel selenide were studied and their application in water, urea, and urine electrolysis were further investigated in detail. This is the first study to utilize $MoSe_2$-based electrode for UOR and elucidate a very slow surface modification of NiSe towards urea electrolysis in the presence of Fe, demonstrating a steadily increasing performance after successive long-term chronopotentiometry analysis. In addition, a rough comparison of the energy requirements for water and urea electrolysis based on the amount of hydrogen gas produced is provided to elucidate the advantages of urea electrolysis over water electrolysis.

Results and Discussion

The synergistically interfaced electrodes were synthesized via a one-step solvothermal reaction (Scheme 1). Nickel foam was used as both Ni precursor and current collector. The selenized nickel foam is identified mainly as NiSe (00-018-0887) and $Ni_{0.85}Se$ (00-018-0888) (Figure 1a and S1). The peaks at 30.88°, 38.47°, 46.52°, 48.05°, 50.23°, 53.57°, 54.94°, and 56.11° are indexed to (3 0 0), (2 1 1), (1 3 1), (4 1 0), (4 0 1), (3 2 1), (3 3 0), and (0 1 2) planes of rhombohedral NiSe (00-018-0887),[18] while the peaks at 16.82°, 33.14°, 44.48°, 59.92°, 61.52°, 69.4°, and 83.22° are indexed to (1 0 1), (1 0 2), (1 1 0), (2 0 1), (2 0 2), and (2 1 1) planes of hexagonal $Ni_{0.85}Se$ (00-018-0888). FS@FO-NS was primarily identified as NiSe and $Ni_{0.85}Se$, with new peaks emerging for $FeSe_2$. Peaks at 34.56°, 57.08°, and 59.49° are indexed to (2 1 0), (2 3 0), and (3 2 1) planes of Cubic $FeSe_2$ (00-048-1881), while peaks at 37.84° and 48.17° are assigned to (2 0 0) and (2 1 1) planes of orthorhombic $FeSe_2$ (00-021-0432). Peaks for cubic Ni_3Se_4 (00-018-0889) are identified at 29.757° and 36.19°, indexed to the (3 1 1) and (4 0 0) planes. One peak at 32.99° is assigned to (2 2 2) plane of cubic Fe_2O_3. For MS-NS, peaks attributed to both rhombohedral NiSe and hexagonal $Ni_{0.85}Se$ were observed with no peaks associated with $MoSe_2$ due to lower concentration and less crystallinity, which was also confirmed from the XRD pattern of MS (Figure S1e).



Scheme 1. Schematic illustration of the synthesis of synergistically interfaced electrodes.

The XPS survey spectra (Figure S1f) indicates the presence of Ni, Fe, Mo, Se, and O elements in the electrodes. The binding energies at 854.86 and 872.72 eV in the Ni $2p_{3/2}$ region of NS (Figure 1b) correspond to Ni^{2+} in Ni–Se and $NiSeO_x$. The presence of SeO_x in $NiSeO_x$ is confirmed from the Se 3d (57.9 eV) spectrum (Figure 1c). While the majority of Ni in NS is present as Ni^{2+}, binding energies at 856.55 and 873.84 eV suggest the presence of Ni^{3+} attributed to surface oxidation and the presence of Ni oxides/(oxy)hydroxides.[20] FS@FO-NS revealed three distinct peaks at binding energies of 853.3, 856.06, and 858.57 eV. The peak at 853.3 eV, which is higher than metallic nickel (852 eV) and lower than nickel oxides (854.5 eV) is attributed to $Ni^{\delta+}$ in Ni-Se.[21] The increased intensity of the Ni^{3+} peak when compared with NS can be a result of the presence of Ni_3Se_4, as evidenced by XRD results and strong electronic interaction between FS@FO and NS within the electrode.[20] These binding energy shifts and appearance of new peaks suggest possible electron transfer between FS@FO and NS.[22,23] The presence of MS resulted in the increased intensity of the Ni–Se peak at 853.24 eV and a decrease in intensity, along with a red shift in the binding energy of the Ni^{2+} peak, indicating the increased metallic nature of MS-NS compared with NS, which endows MS-NS better electronic conductivity and promotes the movement of electrons within the electrode and to the external circuit.

The Se 3d spectrum stipulates the presence of Se^{2-} in metal selenides at binding energies of 53–54.6 eV, and SeO_x at binding energies of 58–58.85 eV.[24,25] An increase in the intensity of the Se^{2-} peak is observed going from NS to FS@FO-NS and MS-NS, indicating FS@FO-NS and MS-NS consist of a more selenized surface than NS. In addition, compared to NS, the Ni 2p and Se 3d peaks of FS@FO-NS and MS-NS are shifted towards lower and higher binding energies respectively, suggesting a strong electronic interaction within the electrodes.[23]

The Fe 2p spectrum of FS@FO-NS (Figure 1d) reveals four peaks, of which binding energies of 706.45 and 720.14 eV reflect the Fe $2p_{3/2}$ and $2p_{1/2}$ of Fe^{2+} in $FeSe_2$ and binding energies at 711.89 and 725.77 eV are attributed to the Fe^{3+} of Fe $2p_{3/2}$ and $2p_{1/2}$ in Fe_2O_3.[23,26–28] The core levels of Mo 3d are observed in the high resolution Mo spectrum (Figure 1e), in which peaks at 228.43 and 231.77 eV are assigned to Mo $3d_{5/2}$ and $3d_{3/2}$ orbitals, confirming that Mo is in its Mo^{+4} and Mo^{+5} state, respectively, in Mo–Se and $MoSe_xO_y$ bonds and the peak at a higher binding energy of 235.32 eV is assigned to Mo^{6+} in MoO_x.[15,23,29–31]

FE-SEM images (Figure 1f–h) revealed a rough uniform surface for NS, while FS@FO-NS is composed of grass-like particles. MS-NS exhibited a heterointerfaced structure in which Ni dominated interconnected nanosheets were surrounded by Mo dominated agglomerated particles. The presence of a heterointerface was confirmed by TEM analysis (Figure 1i–j)

© 2021 Wiley-VCH GmbH

18673899, 2022, 1, Downloaded from https://chemistry-europe.onlinelibrary.wiley.com/doi/10.1002/cctc.202100969 by Hanyang University Library, Wiley Online Library on [19/02/2023]. See the Terms and Conditions (https://onlinelibrary.wiley.com/terms-and-conditions) on Wiley Online Library for rules of use; OA articles are governed by the applicable Creative Commons License

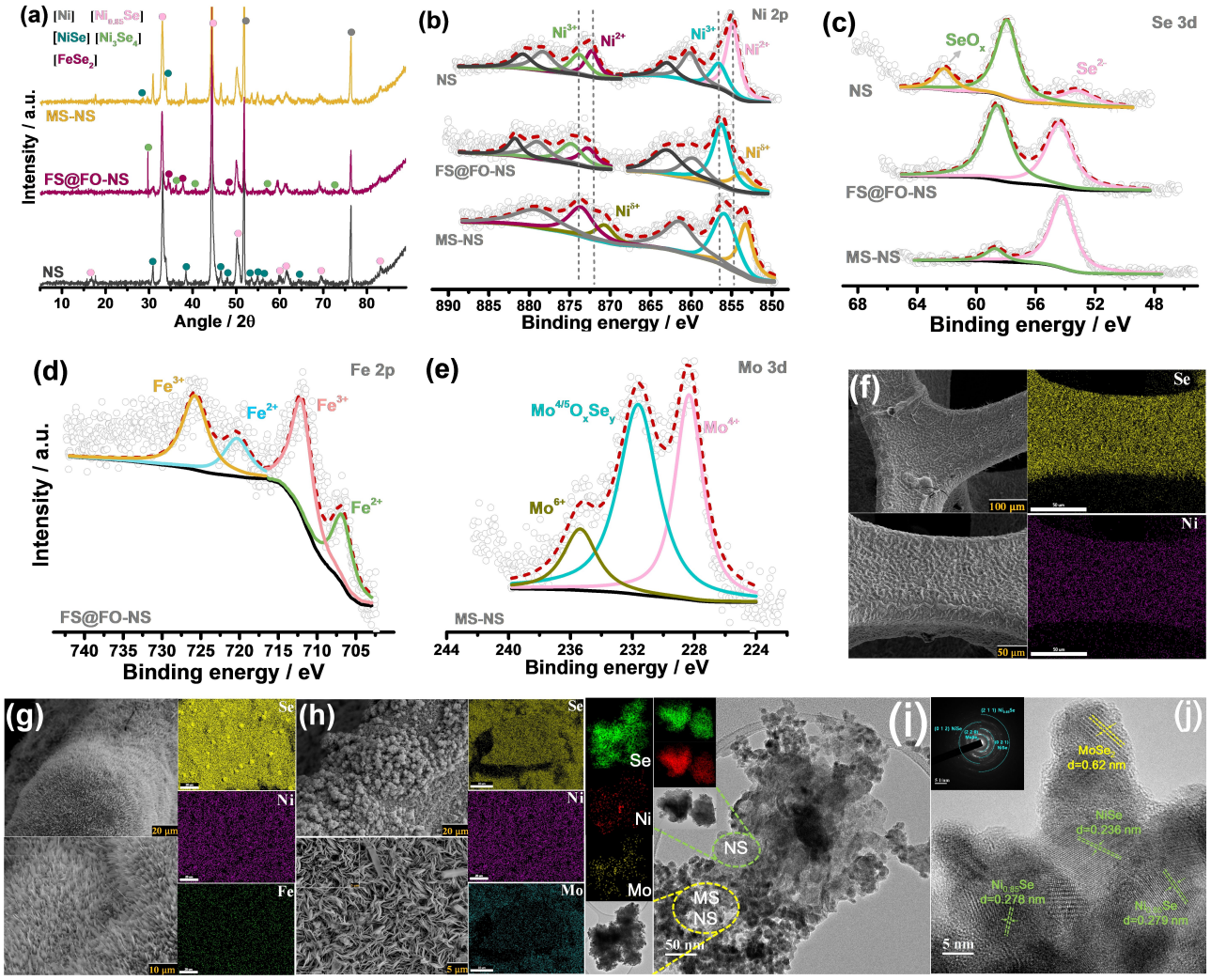


Figure 1. Structural, surface chemistry and morphological analysis of electrodes: (a) XRD; XPS spectrums (b) Ni 2p, (c) Se 3d, (d) Fe 2p, (e) Mo 3d; SEM images and EDS mappings of (f) NS, (g) FS@FO-NS, and (h) MS-NS; (i and j) TEM images and EDS of MS-NS.

wherein Ni rich nanosheets and Mo rich nanoparticles are observed. The EDS analysis (Figure S2–S4) reveals a Ni/Se ratio of 0.82–1.06 and Mo(Fe)/Se ratio of 0.5 for all the electrodes, confirming that the electrodes are composed of NiSe and $Ni_{0.85}Se$, along with $FeSe_2$ and $MoSe_2$.

The HER performance of the electrodes was evaluated in 1 M KOH. NS exhibited poor performance, attaining a current density of −10 and −100 mA cm^{-2} at overpotentials of 184 and 384 mV (Figure 2a). FS@FO-NS showed an improved performance, with overpotentials of 145 and 306 mV at the same current densities. Conversely, MS-NS showed a significantly increased performance, only requiring overpotentials of 97 and 210 mV at current densities of −10 and −100 mA cm^{-2}, respectively (Figure 2b). Powdered monometallic NS, FS@FO, and MS have been analyzed for HER and the polarization curves indicate their poor performance, with NS and MS showing almost similar activities. FS@FO showed the lowest performance. Accordingly, the Tafel analysis (Figure 2c) determined the boost in kinetics of HER in MS-NS, with the lowest Tafel slope of 96 mv dec^{-1}. In addition, MS-NS exhibited a higher DLC value than NS (Figures 2d and S5) which is directly correlated with electrochemically active surface area (Figure S 6a) and suggests the availability of more exposed active sites for H^+ adsorption in MS-NS. The negligible activity difference between NS and MS-NS after ECSA normalization (Figure S6b) highlights the advantage of ECSA in enhancing catalytic activity.[32] Furthermore, MS-NS revealed an increase of one and two orders of magnitude in TOF values (Figure S6c) when compared with FS@FO-NS and NS, respectively, stipulating a more efficient utilization of active sites. The exceptionally high DLC values obtained for FS@FO-NS is a result of the presence of Fe^{II}/Fe^{III} redox couple in the potential window where DLC was calculated. The CV curves of the electrodes (Figure S7) reveal distinct redox peaks for Fe, with the reduction peak in the HER region. Improved HER entails the availability of abundant active sites and their effective utilization via enhanced charge transfer.

ECSA normalized current densities are utilized to identify intrinsic activities of several electrocatalyst.[33–35] Hence the low

© 2021 Wiley-VCH GmbH

18673899, 2022, 1, Downloaded from https://chemistry-europe.onlinelibrary.wiley.com/doi/10.1002/cctc.202100969 by Hanyang University Library, Wiley Online Library on [19/02/2023]. See the Terms and Conditions (https://onlinelibrary.wiley.com/terms-and-conditions) on Wiley Online Library for rules of use; OA articles are governed by the applicable Creative Commons License

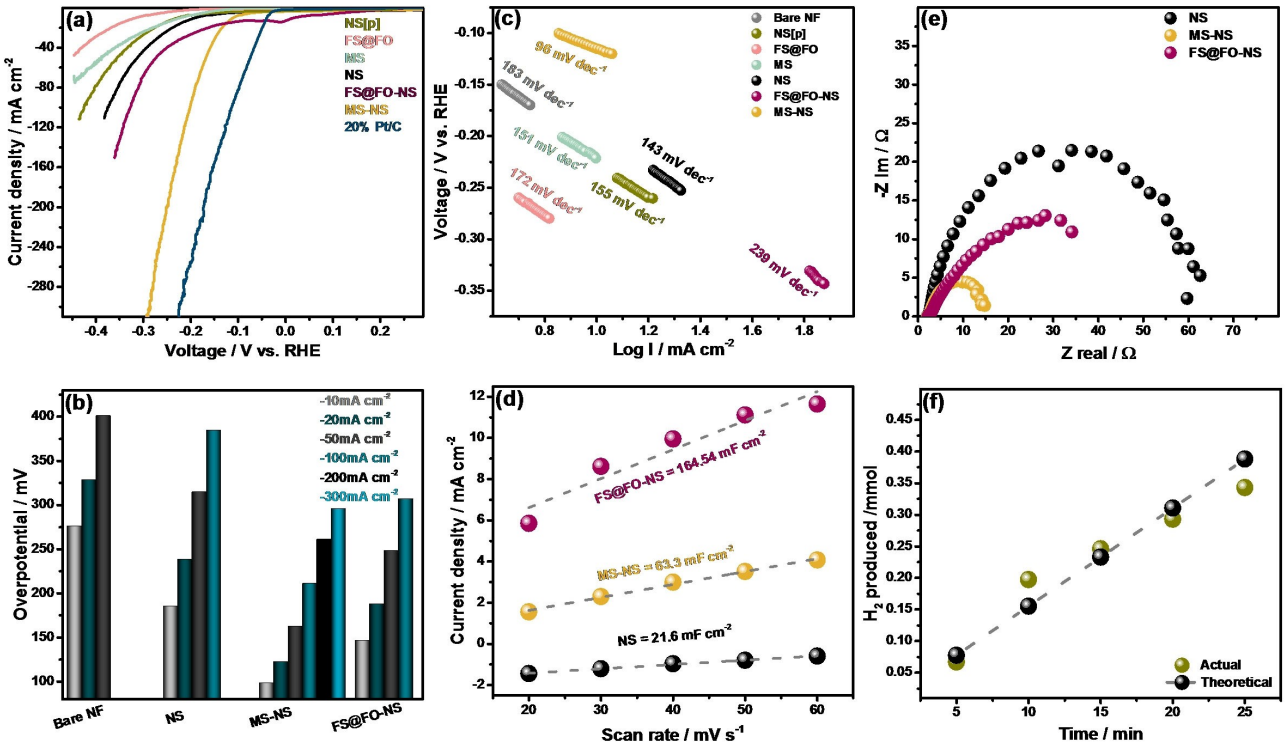


Figure 2. Electrochemical performance for HER: (a) IR corrected polarization curves at a scan rate of 1 mV s^{-1}, (b) Overpotentials at different current densities, (c) Tafel plots, (d) DLC, (e) EIS measurements, and (f) Amount of H_2 gas produced at a constant current density of 50 mA cm^{-2}.

ECSA normalized current density of FS@FO-NS despite its high DLC suggests its poor intrinsic activity for HER. The EIS measurements (Figure 2e) illustrate the improved charge transfer property of FS@FO-NS and MS-NS with smaller semicircle diameters of 50 and 12.5 Ω, respectively, when compared with NS [59.7 Ω] (Figure S8 and Table S1). HER was conducted in acidic (0.5 M H_2SO_4) electrolyte to determine the contribution of each component towards HER in different pH settings. As the polarization curves (Figure S9) indicate, MS-NS showed the best performance, followed by FS@FO-NS and NS, with all the electrodes exhibiting superior performance in alkaline electrolyte to acidic electrolyte. This phenomenon was observed in previous works dealing with Ni-based electrodes for HER.[36] The increased performance in 1 M KOH is explained by the ability of Ni to facilitate water dissociation, which overcomes the rate-determining step for HER in alkaline electrolyzers.[37] To verify this hypothesis, the HER of both monometallic powdered samples and self-supported electrodes were compared in acidic and alkaline electrolytes (Figure S10). From these results NS[p], NS and MS-NS exhibited better performance in alkaline electrolyte, while MS displayed a better performance in acidic electrolyte. The activity trend in acidic solution is mainly influenced by hydrogen adsorption (H_{ad}), and therefore, MS with a large number of exposed active sites for H^+ adsorption is expected to manifest enhanced HER in an acidic environment. However, water dissociation (Volmer step) dominates the overall reaction rate in an alkaline medium in addition to H^+ adsorption and as such, a favorable H/OH adsorption with low water dissociation barrier is required. In this regard, Ni promotes the dissociation of water by the favorable interaction with hydroxyl,[36], resulting in a boosted HER in alkaline electrolyte.

Finally, the long-term performance of MS-NS was analyzed in alkaline electrolyte at a current density of −20 mA cm^{-2} for 12 h (Figure S11a). The polarization curves before and after 12 h of continuous CP (Figure S11b) show a negligible difference, thereby displaying a stable performance. A constant current of 50 mA cm^{-2} was applied to the system and the amount of hydrogen production on MS-NS was measured with an online gas chromatography revealing a 98.3% faradaic efficiency (Figure 2f).

Water oxidation in the absence [1 M KOH] and presence [1 M KOH + 0.33 M urea] of urea was conducted, and the polarization curves are given in Figures 3a and 4a, respectively. Similar to previously reported transition metal chalcogenides for water oxidation.[10,13,35,36] An initial electrochemical activation was observed under anodic treatment at ~1.4 V vs. RHE, which is attributed to the $Ni^{2+/3+}$ transformation. Therefore, the polarization curves were swept from higher potentials (Figure S12a) to negate the effects of the current from Ni oxidation while computing overpotentials at different current densities. From the cyclic voltammetry (Figure S12b), NS exhibited a large anodic oxidation peak, while the oxidation peak for MS-NS was shifted to a lower potential, indicating the ease of oxidation of Ni in the presence of Mo. However FS@FO-NS, with the lowest redox peak area suppressed the oxidation of Ni keeping it in a Ni^{2+} state. FS@FO-NS displayed the best performance for OER,

© 2021 Wiley-VCH GmbH

18673899, 2022, 1, Downloaded from https://chemistry-europe.onlinelibrary.wiley.com/doi/10.1002/cctc.202100969 by Hanyang University Library, Wiley Online Library on [19/02/2023]. See the Terms and Conditions (https://onlinelibrary.wiley.com/terms-and-conditions) on Wiley Online Library for rules of use; OA articles are governed by the applicable Creative Commons License

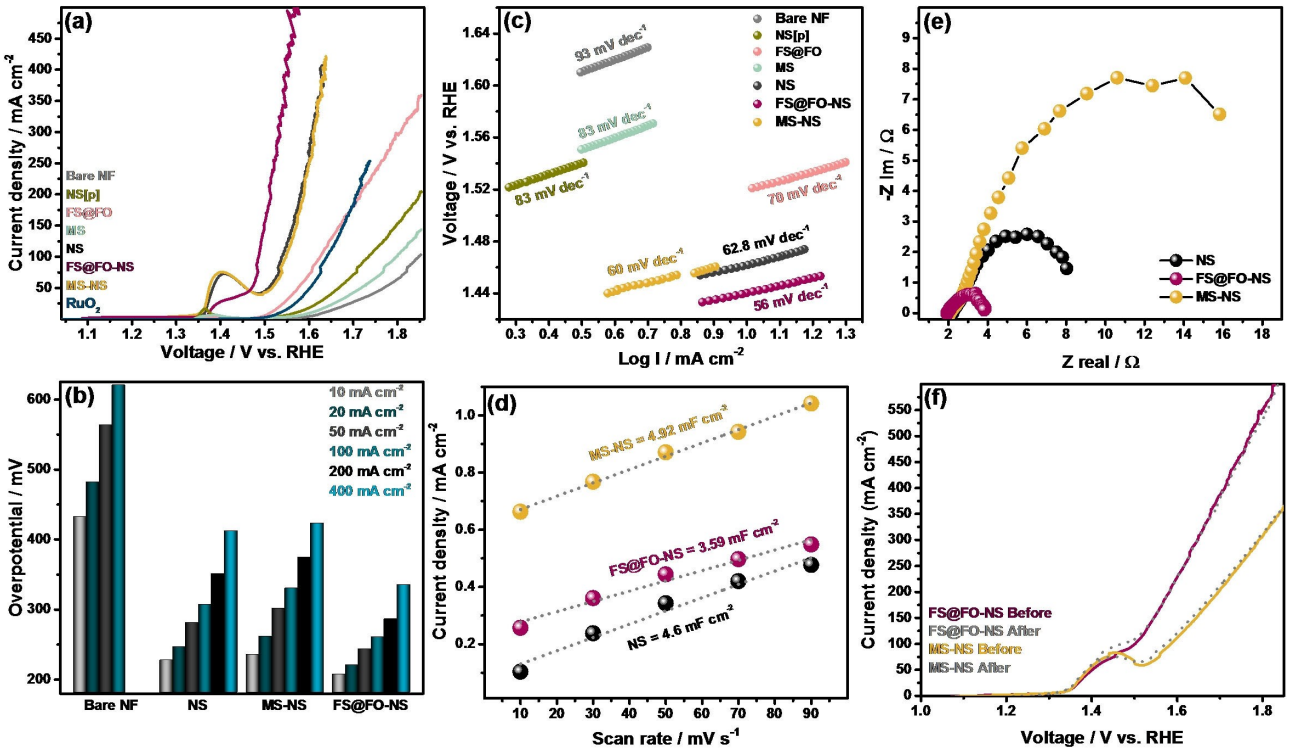


Figure 3. Electrochemical performance for OER: (a) IR corrected polarization curves at a scan rate of 1 mV s^{-1}in 1 M KOH, (b) Overpotentials at different current densities, (c) Tafel plots, (d) DLC analysis, (e) EIS measurements, (f) Polarization curves after CP analysis @ 20 mA cm^{-2} for 12 h.

attaining a current density of 10, 100, and 400 mA cm^{-2} at overpotentials of 206, 250 and 330 mV. NS attained the same current densities with overpotentials of 225, 306 and 411 mV. MS-NS did not produce any enhancement on OER performance and exhibited the same overpotentials as NS. Previous studies have considered NiOOH to be the active site and its formation at lower overpotentials is sought for boosting OER kinetics.[22,39,40] However, in the present study, FS@FO-NS exhibited the highest performance despite the suppressed oxidation of Ni, while MS-NS with enhanced Ni oxidation did not improve the OER performance. This is because different active sites were observed for Ni based electrodes containing Fe and other transition metals. While lattice oxygen is involved in the OER for Ni based electrodes evolving oxygen via a $NiOO^{-}$ species by the deprotonation of NiOOH, the incorporation of Fe significantly increases the activity by changing the nature of active sites[41] and enhancing charge transfer properties[13] . In addition, sever oxidation of electrodes might lead to the formation of a thick oxide/(oxy)hydroxide layer on the electrode surface which might result in increased charge transfer resistance.[39] Even extremely thin (oxy) hydroxide films were observed to exhibit significant overpotentials due to their poor conductivity.[40] Therefore, Fe can effectively regulate the electronic properties of FS@FO-NS by keeping Ni oxidation at bay. This assumption is confirmed by the Tafel, DLC and EIS results (Figure 3c–e, and S13). FS@FO-NS exhibits the lowest Tafel slope and the highest activity in contrast to its low ECSA while displaying the lowest charge transfer resistance, which indicates its pronounced role towards the efficient utilization of available active sites through improved charge transfer capability. The ECSA normalized polarization curves and TOF results (Figure S14) confirm the proposed effective utilization of active sites by FS@FO-NS, with two orders of magnitude increase in TOF. In addition, the shift in the phase degree peak to a higher frequency direction for FS@FO-NS in the Bode plot (Figure S22a) suggests faster OER kinetics as a result of fast charge transfer.[11] However, MS-NS resulted in an increased charge transfer resistance, with the largest semicircle radius of 16.2 Ω, while NS and FS@FO-NS showed a very low resistance of 5.7 and 1.33 Ω (Figure S15 and Table S2). The increased charge transfer resistance of MS-NS is attributed to the generation of a large amount of $Ni(OH)_2$/NiOOH layer during OER, which acts as an insulating layer.[22] The activity of monometallic powdered NS, FS@FO, and MS for OER were investigated and compared with the self-supported electrodes directly grown on nickel foam. The powdered monometallic NS and MS exhibited significantly low activity compared with the self-supported synergistically interfaced electrodes (Figure 3a). This is attributed to the enhanced electrolyte penetration and the ability of the 3D nickel foam to efficiently expose active sites and synergistic interaction between components compared with powdered samples drop-casted on nickel foam. In contrast, FS@FO exhibited an exceedingly good performance among the powdered monometallic electrocatalysts by achieving a current density of 10 and 100 mA cm^{-2} at an overpotential of 280 and 353 mV, while NS and MS required significantly higher overpotentials (356 and

© 2021 Wiley-VCH GmbH

18673899, 2022, 1, Downloaded from https://chemistry-europe.onlinelibrary.wiley.com/doi/10.1002/cctc.202100969 by Hanyang University Library, Wiley Online Library on [19/02/2023]. See the Terms and Conditions (https://onlinelibrary.wiley.com/terms-and-conditions) on Wiley Online Library for rules of use; OA articles are governed by the applicable Creative Commons License

519 mV) and (368 and 553 mV), respectively, at the same current densities.

These results suggest that Fe provides most of the active sites for OER along with high valence $Ni^{3+/4+}$, whose formation is induced as a result of Fe incorporation. In addition, both FS@FO-NS and MS-NS displayed a stable performance for 12 h at a current density of 20 mA cm^{-2}, with negligible activity loss (Figures 3f and S16).

The UOR performance of the electrodes was investigated in 1 M KOH aqueous electrolyte containing 0.33 M urea. After introducing 0.33 M urea, MS-NS showed a substantially enhanced performance, with rapid current density rise because of more favorable UOR than OER when compared with NS (Figure 4a). The favorable kinetics of UOR over OER on MS-NS is shown by the highest current contribution of urea (68.1%) when compared with NS (44.81%) and FS@FO-NS (33.25%) at 1.55 V vs. RHE (Figure S17). The decline in the urea contribution as the potential is increased results from the competition between OER and UOR at potentials beyond 1.55 V vs. RHE. As observed in previous works[11,42] hydroxyl ion adsorption prevails at higher applied voltage, assisting in the removal of adsorbed CO_2 and stabilizing it in the form of a carbonate ion (CO_3^{2-}) in the electrolyte. The presence of CO_3^{2-} ions in the electrolyte after UOR is confirmed by the FTIR spectra of the spent electrolyte (Figure S18). The presence of metal carbonate species after UOR was confirmed by Raman analysis for MS-NS and FS@FO-NS (Figure S19). Moreover, GC analysis of the produced gases revealed the absence of CO_2 gas in the gas mixture indicating the adsorption and reaction of CO_3^{2-}specis on the electrode surface[8] inhibiting its release as a gas product. While the difference in the polarization curves of FS@FO-NS for OER and UOR was minimal without IR correction (Figure S20a–c), after 90% IR correction, all three electrodes displayed improved performance in the presence of urea (Figure S20d–f). The potential at a current density of 100 mA cm^{-2} shifted from 1.49 and 1.56 V vs. RHE to 1.42 V vs. RHE for FS@FO-NS and MS-NS, 70 and 140 mV lower than in the absence of urea, respectively, strongly highlighting the better energy conversion efficiency (Figure 4b). NS required a relatively high potential of 1.47 V. Comparing the difference in OER and UOR performances of FS@FO-NS and MS-NS shows that the formation of NiOOH is a mandatory step and primary active site for UOR because the onset of UOR coincides well with the onset of Ni^{2+}/Ni^{3+} transition. The $Ni^{2+/3+}$ transformation is expedited by urea according to the Electrochemical-Chemical (E-C) process.[11]

$$NiOH_2 + OH^- \leftrightarrow NiOOH + H_2O + e^- \quad (4)$$

$$6NiOOH + CO(NH_2)_2 + H_2O \rightarrow 6Ni(OH)_2 + N_2 + CO_2 \quad (5)$$

The current crossover at around 1.34 V vs. RHE (Figure S21a) in the presence of urea suggests in-situ surface reconstruction during CV that serves to activate the material during each cycle.[43] The weak reduction peaks of NiOOH to $NiOH_2$ in the presence of urea (Figure S21b–d) is due to an indirect urea oxidation process which consumes part of NiOOH active sites.[11]

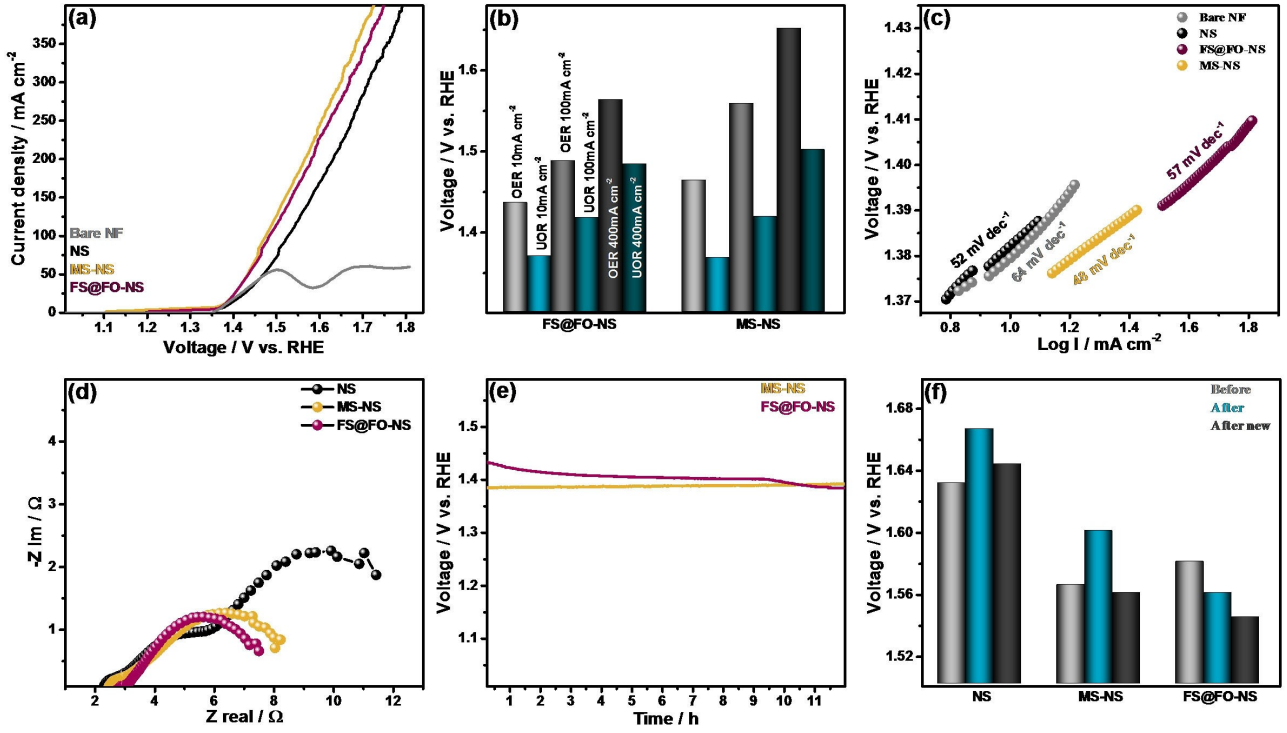


Figure 4. Electrochemical performance for UOR: (a) IR corrected polarization curves at a scan rate of 1 mV s^{-1}in 1 M KOH + 0.33 M urea,, (b) Potentials at different current densities as compared with OER, (c) Tafel plots, (d) EIS measurements, (e) CP analysis @ 20 mA cm^{-2} for 12 h, and (f) Potentials @ 50 mA cm^{-2} before and after CP (new refers to new electrolyte).

© 2021 Wiley-VCH GmbH

18673899, 2022, 1, Downloaded from https://chemistry-europe.onlinelibrary.wiley.com/doi/10.1002/cctc.202100969 by Hanyang University Library, Wiley Online Library on [19/02/2023]. See the Terms and Conditions (https://onlinelibrary.wiley.com/terms-and-conditions) on Wiley Online Library for rules of use; OA articles are governed by the applicable Creative Commons License

Moreover, the lower Tafel slopes for bare NF, NS, and MS-NS (Figure 4c) illustrate the improved kinetics of UOR when compared with OER, while FS@FO-NS maintained the same Tafel slope for both OER and UOR.

The EIS measurements (Figure 4d) clearly exhibit the changes of ionic and electronic resistances of the electrodes. The radius of the semicircle of FS@FO-NS and MS-NS is smaller than that of NS, indicating that FS@FO-NS and MS-NS have a higher charge-transfer rate and thereby a more rapid UOR kinetics.[44] The presence of an additional semi-circle in the low frequency region for NS, which is related to the changing concentration of charged intermediates (*COO^-), was observed.[45] This semi-circle was only observed for NS in the presence of urea, revealing that there is an increased resistance as a result of desorption of charged species from the surface of NS, possibly due to strong *COO adsorption. The bode plots (Figure S22b) reveal a pseudo semi-circle at high frequency regions for NS and MS-NS corresponding to the resistance as a result of an insulating $Ni(OH)_2$.[22] This pseudo semi-circle is not present for FS@FO-NS, in keeping with the suppressed Ni oxidation.

CO/CO_2 poisoning is a major problem for UOR electrocatalysts, hindering their long-term utilization,[10] and therefore, CP measurements were conducted for all the electrodes at a current density of 20 mA cm^{-2} for 12 h (Figure 4e) and polarization curves were recorded in spent and new electrolytes. From the polarization curves after CP (Figure S23), replenishing the electrolyte restored some of the activity, suggesting a portion of activity loss is due to limited availability of urea in the electrolyte. After CP, NS and MS-NS displayed an increase, while FS@FO-NS showed a decrease in potential. These results, when compared with bare NF that retained only 50% of its initial current density after 2 h of operation (Figure S24), suggest that Se and Mo improve the anti-poisoning effect by regulating the electronic structure of Ni and hindering CO_2 poisoning,[46] while a slow surface activation/reconstruction takes place on the FS@FO-NS during UOR, resulting in an improved performance after long-term CP analysis. The decrease in potential for FS@FO-NS after CP is observed only in the case of UOR. The HER performance was measured in 1 M KOH + 0.33 M urea revealing a negligible interference of urea on HER (Figure S25).

To probe the nature of active sites for the three reactions the XPS of fresh and spent electrodes were analyzed and compared (Figure 5 and S26). The formation of an active unsaturated oxyselenide phase was elucidated for HER as a result of an irreversible reduction of Mo^{6+} species and partial dissolution of Mo–Se during the first few LSV scans as confirmed by the ICP-OES analysis of the spent electrolyte (Table S3). Moreover, the formation of an oxidized Ni species due to the adsorption of OH^- ions on Ni sites during HER was also observed, further confirming Ni as the active site for water dissociation (Scheme 2a). A Ni^{3+} rich surface was observed for Post OER/UOR NS and MS-NS, while a Ni^{2+} rich surface was observed for post OER/UOR FS@FO-NS with the presence of abundant Fe^{3+} species (Figure S29) confirming the suppression of $Ni^{2+/3+}$ transition. In addition, even though Fe suppresses Ni oxidation, the formation of γ-NiOOH with a mixed valence of

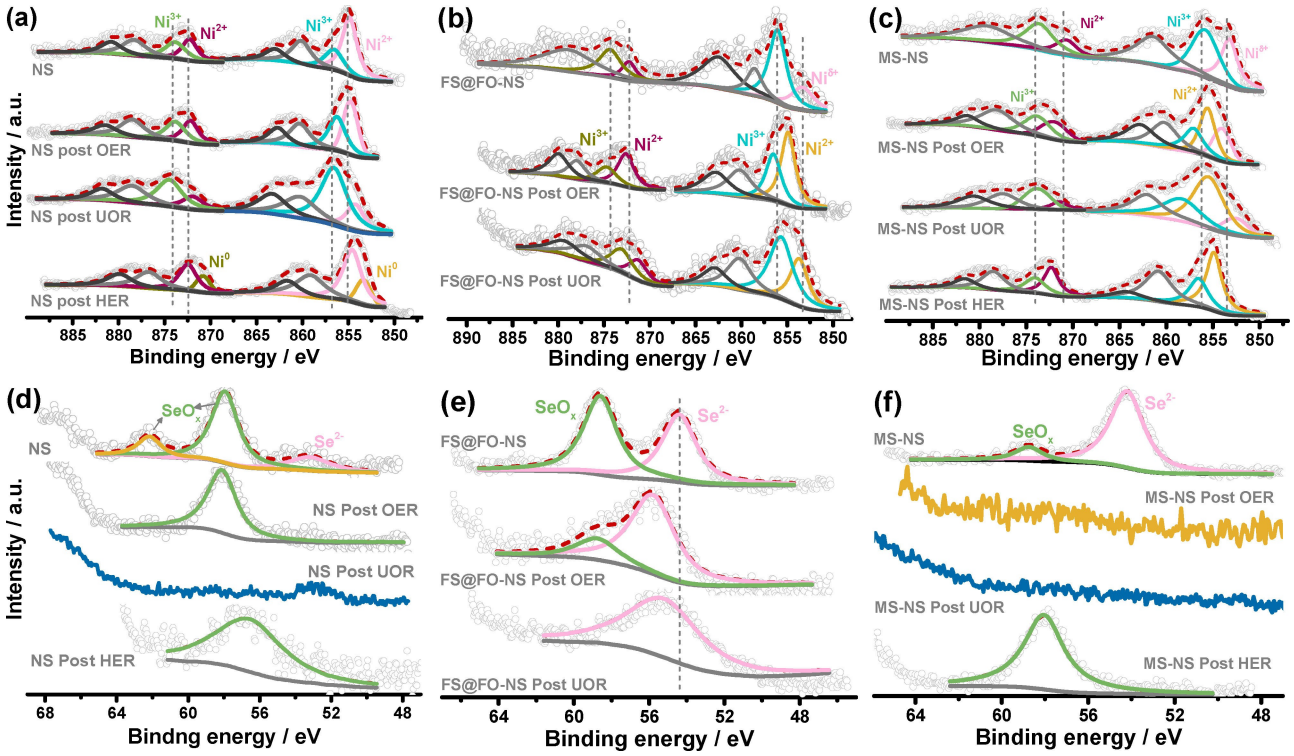
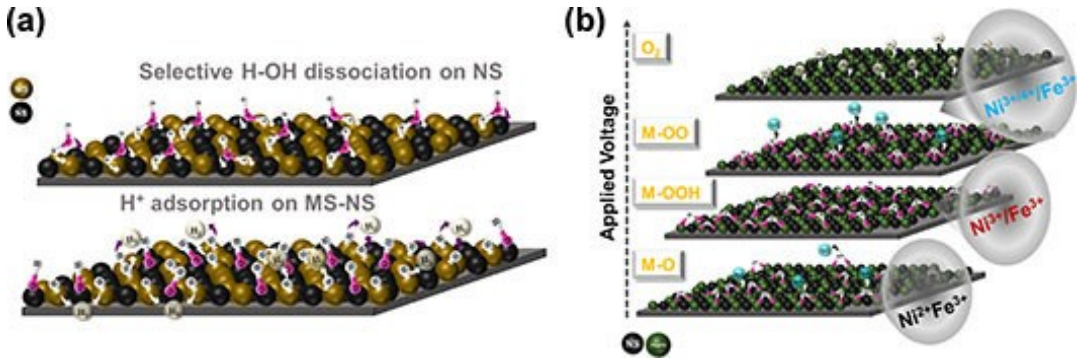


Figure 5. Pre and Post reaction XPS analysis: (a–c) Pre and Post reaction Ni 2p spectrums for NS, MS-NS and FS@FO-NS; (d–f) Pre and post reaction Se 3d spectrums for NS, MS-NS and FS@FO-NS

© 2021 Wiley-VCH GmbH

18673899, 2022, 1, Downloaded from https://chemistry-europe.onlinelibrary.wiley.com/doi/10.1002/cctc.202100969 by Hanyang University Library, Wiley Online Library on [19/02/2023]. See the Terms and Conditions (https://onlinelibrary.wiley.com/terms-and-conditions) on Wiley Online Library for rules of use; OA articles are governed by the applicable Creative Commons License



Scheme 2. Schematic illustration of the proposed steps for (a) HER on MS-NS and (b) OER on FS@FO-NS

$Ni^{3+/4+}$ at higher applied potentials (> 1.5 V vs. RHE) was confirmed by Raman analysis for FS@FO-NS (Figure S30 and Scheme 2b). γ-NiOOH is reported to be more active than β-NiOOH (Ni^{3+}) for OER.[47] [Detailed discussions for XPS and Raman analysis are provided in the electronic supplementary information].

The overall water and urea electrolysis reactions were investigated in a two-electrode setup with different electrode configurations in the absence and presence of urea, respectively. FS@FO-NS//MS-NS exhibited the best performance for water electrolysis with 1.56 V at 10 mA cm^{-2}, while MS-NS//MS-NS and FS@FO-NS//FS@FO-NS required a higher potential of 1.59 and 1.62 V, respectively (Figure 6a and b). In contrast, MS-NS//MS-NS recorded the lowest cell voltage of 1.27 V for urea electrolysis at 10 mA cm^{-2} (Figure 6d and e). This value is the lowest potential reported for urea electrolysis to date (Table S6). FS@FO-NS//FS@FO-NS and FS@FO-NS//MS-NS attained the same current densities at a significantly higher cell voltages of 1.48 and 1.37 V, respectively.

These bifunctional electrodes also demonstrated an impressive long-term performance, with negligible activity loss for both water (Figure S32 and 6C) and urea electrolysis (Figure 6f) at a current density of 50 mA cm^{-2}. While MS-NS//MS-NS displayed a slight increase in cell voltage after 24 h of continuous urea electrolysis at 50 mA cm^{-2}, FS@FO-NS//FS@FO-NS and FS@FO-NS//MS-NS revealed a continuous decrease in cell voltage even after 48 and 72 h of continuous electrolysis at the same current density. This resulted in a very durable cell performance for three and four days, respectively (Figure 6g and S33). Fresh MS-NS//MS-NS and FS@FO-NS//MS-NS after 72 h of CP were observed to have an almost overlapping polarization curve and cell voltage (Figure S34). A small increase in cell voltage is observed after 48 and 100 h of urea electrolysis for FS@FO-NS//FS@FO-NS and FS@FO-NS//MS-NS, respectively. However, the cell potential remained lower than that for the fresh electrodes. To understand the decrease in cell voltage for urea electrolysis following CP, the nature of the electrodes (for configurations of MS-NS//MS-NS and FS@FO-NS//MS-NS) at 24 h interval after CP were studied using XRD (Figure 6h and I and S35–37). The XRD patterns of MS-NS (anode) in MS-NS//MS-NS configuration after 24 h of urea electrolysis (Figure S35) revealed major changes of decreased peak intensities, and the shifting, broadening and disappearance of peaks linked to NiSe and $Ni_{0.85}Se$. These changes are attributed to the reconstruction/transformation of NiSe and $Ni_{0.85}Se$ to an amorphous $Ni(OH)_2$ phase. In contrast, the anode [FS@FO-NS] in FS@FO-NS//MS-NS configuration displayed few new peaks attributed to FeOOH and nickel hydroxide hydrate [$3Ni(OH)2 \cdot 2H_2O$ (00-022-0444) after 24 h CP, along with the disappearance of $FeSe_2$ diffraction peaks, while maintaining the peaks of NiSe (Figure 6h). The intensity of these new peaks increase after 48 h of CP, while additional peaks with increased intensity attributed to nickel hydroxide hydrate and $Ni(OH)_2$ (01-073-1520) were detected after 72 h of CP (Figure S37). After 100 h of CP, the electrode was dominated by amorphous species with only a few sharp peaks remaining.

That the minimum voltage for urea electrolysis for the FS@FO-NS//MS-NS configuration is attained after 72 h of CP, along with the presence of abundant $Ni(OH)_2$ species from the XRD results, suggests a slow surface reconstruction-induced activation for FS@FO-NS. This resulted in an improved performance, with successive CPs at a relatively high current density, establishing $Ni(OH)_2$ as the active site for UOR. In contrast to the anodes, the MS-NS cathode in both MS-NS//MS-NS and FS@FO-NS//MS-NS configuration did not display any change in the XRD patterns up to 100 h of urea electrolysis except for the appearance of few new peaks ascribed to Ni_3Se_2 (Figure 6i and S37e). These results suggest a rapid amorphization and transformation of MS-NS to $Ni(OH)_2$ and a slow surface reconstruction-induced activation for FS@FO-NS anode while no apparent change was observed for the MS-NS cathode (Figure S36) illustrating that the enhanced activity of FS@FO-NS//MS-NS after CP is solely due to the dynamic reformation of the anode.

UOR and urine electrolysis were conducted in human urine containing 1 M KOH (Figures S38 and 39). The UOR results revealed comparable activity with 1 M KOH containing urea, with slight increase in potential, due to the lower urea concentration in urine.[48] To illustrate the potential towards coupled waste treatment and hydrogen generation, urine electrolysis in urine with 1 M KOH was conducted (Figure 7 a and b). Although the polarization curves reveal higher cell voltages for urine compared with urea, urine electrolysis

© 2021 Wiley-VCH GmbH

18673899, 2022, 1, Downloaded from https://chemistry-europe.onlinelibrary.wiley.com/doi/10.1002/cctc.202100969 by Hanyang University Library, Wiley Online Library on [19/02/2023]. See the Terms and Conditions (https://onlinelibrary.wiley.com/terms-and-conditions) on Wiley Online Library for rules of use; OA articles are governed by the applicable Creative Commons License

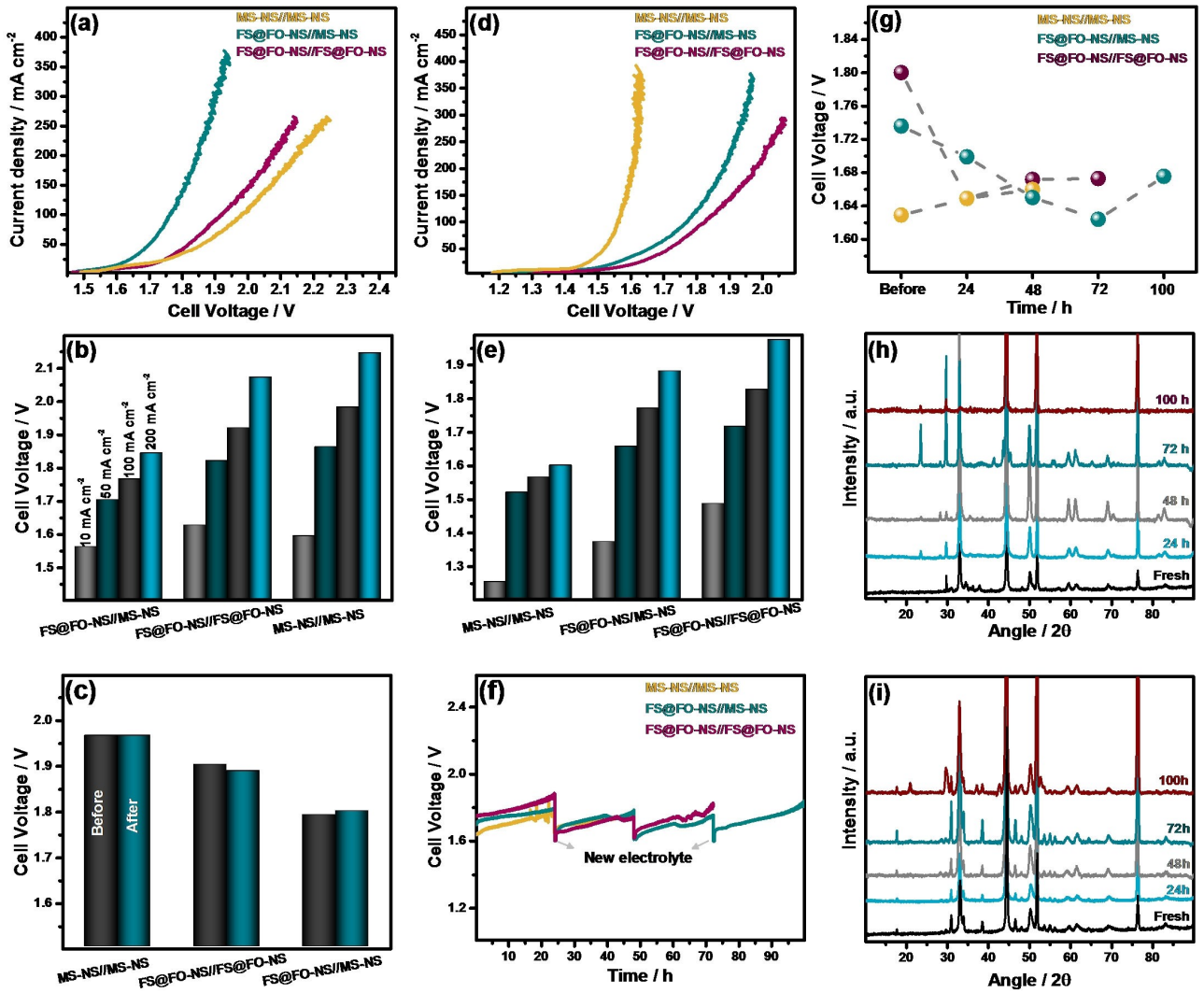


Figure 6. Water electrolysis results [a–c]: (a) Polarization curves at a scan rate of 1 mV s^{-1} in 1 M KOH, (b) Potentials at different current densities, (c) Potential at 50 mA cm^{-2} before and after CP analysis; Urea electrolysis results [d–i]: (d) Polarization curves at 1 mV s^{-1} in 1 M KOH + 0.33 M urea, (e) Potential at different current densities, (f) CP analysis for 2–4 days at 50 mA cm^{-2}, (g) Cell voltage after CP analysis at 50 mA cm^{-2} for urea electrolysis for different electrode configurations in new electrolyte, Post Urea electrolysis XRD patterns after CP at 50 mA cm^{-2} at different time intervals: (h) XRD patterns of FS@FO-NS anode in the FS@FO-NS//MS-NS configuration and (i) XRD patterns of MS-NS cathode in the FS@FO-NS//MS-NS configuration.

displayed lower cell voltage than water electrolysis with vigorous gas bubbling. FS@FO-NS//MS-NS displayed poor urine electrolysis (Figure S40), while MS-NS//MS-NS revealed excellent activity, delivering a current density of 200 mA cm^{-2} at 1.9 V and demonstrating the potential for real life applications and a new avenue towards low-cost sustainable energy. Unfavorable interactions of Fe^{III} centers with other organic molecules in urine, specifically uric acid (UA) is hypothesized to be the main reason for the poor urine electrolysis of FS@FO-NS//MS-NS (Figure S41). Fe has been extensively reported as an electrochemical sensor for UA,[49–52] where there is a uric acid-led reduction of Fe^{3+} to Fe^{2+}, weakening the role of Fe in suppressing $Ni^{2+/3+}$ transformation. The presence of a large amount of pale green matter on the surface of FS@FO-NS, after urine electrolysis supports this assumption by revealing a severely oxidized surface of $Ni(OH)_2$ (Figure S42). The significant increase in the charge transfer resistance of FS@FO-NS couple for urine electrolysis compared with water and urea electrolysis (Figure S43) also indicates the impaired kinetics of urine electrolysis as a result of limited charge and electron transfer capability due to overoxidation.

The amount of H_2 gas produced for both water and urea electrolysis was quantified using an online-gas chromatography connected with the two-electrode setup (Figure 7c). Hydrogen and oxygen gas were detected for water electrolysis while the production of hydrogen and nitrogen gases were confirmed for urea electrolysis (Figure 7d). These results suggest that UOR is the dominant process at the anode with effective suppression of OER. The amount of H_2 produced per applied voltage showed a 1.6 fold increase for urea electrolysis when compared with water electrolysis (Figure 7e) along with a 37% decrease in

© 2021 Wiley-VCH GmbH

18673899, 2022, 1, Downloaded from https://chemistry-europe.onlinelibrary.wiley.com/doi/10.1002/cctc.202100969 by Hanyang University Library, Wiley Online Library on [19/02/2023]. See the Terms and Conditions (https://onlinelibrary.wiley.com/terms-and-conditions) on Wiley Online Library for rules of use; OA articles are governed by the applicable Creative Commons License

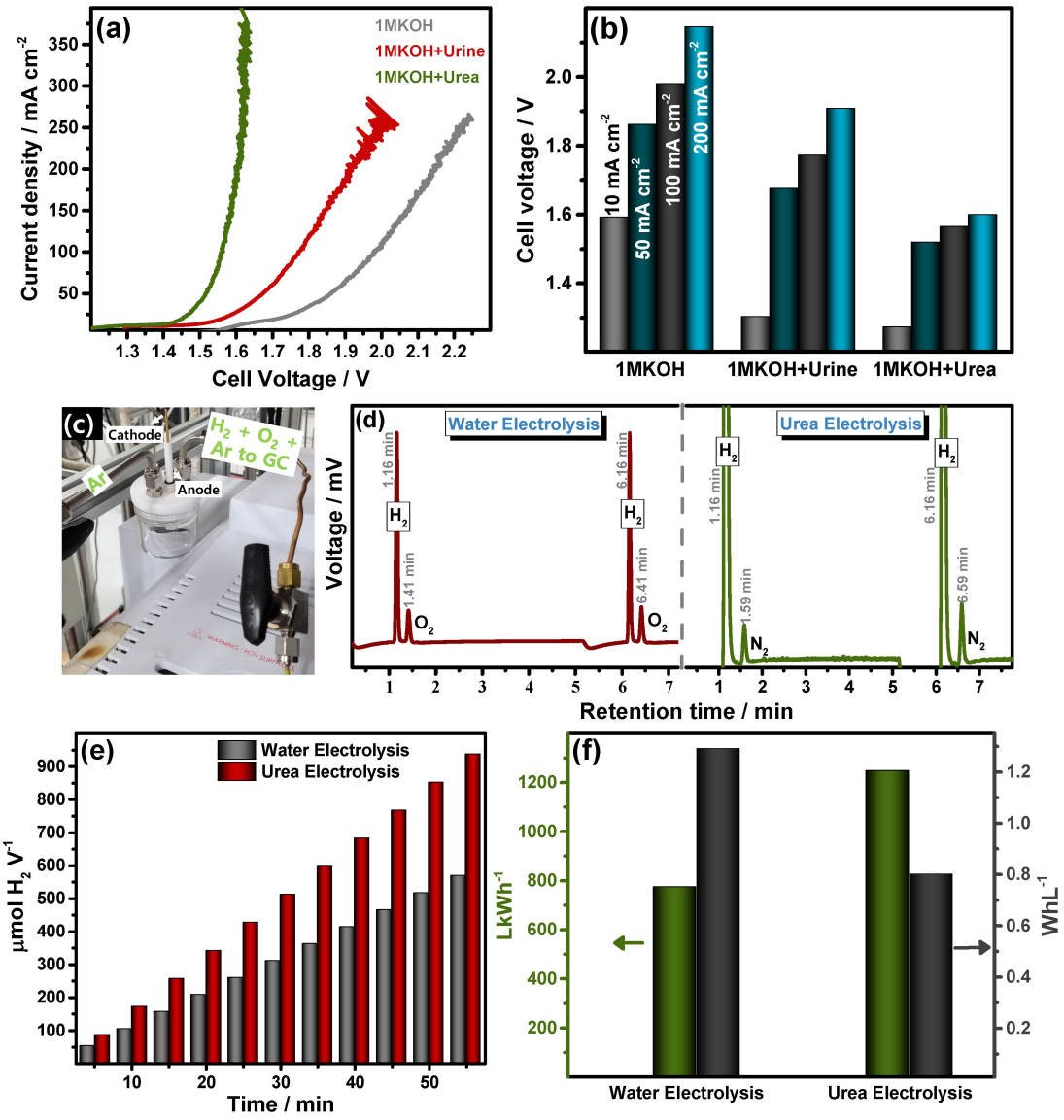


Figure 7. Urine electrolysis results: (a) Polarization curves of MS-NS//MS-NS in different electrolytes, (b) Overpotentials of MS-NS//MS-NS configuration at different current densities for water urea and urine electrolysis; Gas chromatography results for the produced gases during water and urea electrolysis : (c) picture of the setup used to analyse the produced gases in a two electrode system connected with an online gas-chromatogram, (d) The gas chromatograms for water and urea electrolysis, (e) comparison of amount of H_2 produced per applied voltage for water and urea electrolysis and (f) comparison of the power consumption for hydrogen production for water and urea electrolysis.

the power consumption of the electrolyzer (Figure 7f) illustrating the advantages of urea electrolysis.

Conclusion

In this work the diametrically opposed effects of Fe and Mo on the activity of NS towards HER, OER, and UOR, along with overall water and urea electrolysis have been studied in detail. From electrochemical analysis and Physico-chemical characterizations, the following conclusions are drawn. (1) The high HER performance of MS-NS in alkaline electrolyte is attributed to the coupled effects of low energy requirement for water dissociation by NS and abundant active sites and high TOF of MS. (2) FS@FO-NS equipped with fast charge transfer capability exhibited the highest OER activity through effective active site utilization. At low applied potentials, Fe^{3+} in FeOOH serves as an active site for intermediate adsorption, while at higher applied potentials $Ni^{+3.6}$ in γ-NiOOH facilitates charge transfer resulting in a boost in OER kinetics. (3) The fresh MS-NS//MS-NS exhibited the highest performance for urea electrolysis as a result of fast active site generation because of Mo. This fast activation gave rise to a continuous increase in cell voltage with successive CPs due to slow CO_2 desorption kinetics as a result of strong binding of CO_2 to $Ni(OH)_2$[7] and increased charge transfer resistance. (4) FS@FO-NS//MS-NS and FS@FO-NS//FS@FO-NS exhibited a continuous and notable activity enhancement, with successive CPs due to slow surface trans-

© 2021 Wiley-VCH GmbH

18673899, 2022, 1, Downloaded from https://chemistry-europe.onlinelibrary.wiley.com/doi/10.1002/cctc.202100969 by Hanyang University Library, Wiley Online Library on [19/02/2023]. See the Terms and Conditions (https://onlinelibrary.wiley.com/terms-and-conditions) on Wiley Online Library for rules of use; OA articles are governed by the applicable Creative Commons License

formation because of suppressed Ni oxidation by Fe. This slow activation endowed FS@FO-NS with an optimized UOR intermediate energetics while maintaining a highly conductive scaffold for charge and electron transfer for a long period of time. The urine electrolysis has also demonstrated the potential of these materials for real life applications in regard to low-cost clean energy generation coupled with waste treatment.

Experimental Section

Chemicals: Iron nitrate nonahydrate [$Fe(NO_3)_2 \cdot 9H_2O$, (99%)] was purchased from Sigma Aldrich. Nickel nitrate hexahydrate [$Ni(NO_3)_2 \cdot 6H_2O$, (99%)], ammonium heptamolybdate tetra hydrate [$(NH_4)_6Mo_7O_{24} \cdot 4H_2O$, (99%)], elemental selenium (99%), hydrazine hydrate, 55% (hydrazine, 33.5%), sodium hydroxide [NaOH, (99%)], potassium hydroxide [KOH, (85%)], urea and commercial RuO_2 were purchased from Acros organics. NN-dimethyl formamide and Ni foam, with a thickness of 1.6 mm were purchased from Daejung chemicals and MTI Korea, respectively. All chemicals were used without any further purification. Deionized water and ethanol were used for solution preparation and washing purposes, respectively.

Synthesis of NiSe: Self-supported NiSe was synthesized via a modified one-step solvothermal approach (Scheme 1). Prior to synthesis, Ni foam was ultrasonically cleaned in 1 M HCl, deionized water, and ethanol successively, for 20 min each and dried at 80 C for further use. Under strong stirring, 0.3 g of sodium hydroxide was dissolved in 25 mL DMF, followed by the addition of 3.75 mmol of Se and 140 μL of hydrazine hydrate. After stirring for 3 h, the solution was transferred to a 100 mL Teflon lined stainless steel autoclave. The cleaned nickel foam, mounted on a glass substrate with the aid of Teflon tape, was immersed in the solution with a tilted angle against the wall facing down. The autoclave was then sealed and maintained at 180 °C for 12 h. The obtained NiSe was ultrasonically cleaned in water and ethanol for 5 min, respectively and dried at 60 °C for 6 h.

Synthesis of $FeSe_2$@Fe_2O_3/NiSe and $MoSe_2$/NiSe: The $FeSe_2$@Fe_2O_3-NiSe and $MoSe_2$-NiSe electrodes were synthesized following the same procedure as NiSe with the addition of iron nitrate nonahydrate [$Fe(NO_3)_2 \cdot 9H_2O$] and ammonium heptamolybdate tetra hydrate [$(NH_4)_6Mo_7O_{24} \cdot 4H_2O$], respectively. The electrodes will be referred to as NS ($Ni_{0.85}Se$), FS@FO-NS ($FeSe_2$@Fe_2O_3/NiSe) and MS-NS ($MoSe_2$/NiSe) throughout the study.

The monometallic powdered samples were synthesized by following the same procedure without using nickel foam as a substrate and are designated as NS[p] ($Ni_{0.85}Se$), FS@FO ($FeSe_2$@Fe_2O_3) and MS ($MoSe_2$).

Acknowledgements

This work was supported by the National Research Foundation of Korea (NRF) grant funded by the Korea government (MSIT) (No. 2020R1A5A1019131 and No. 2019R1A2C1090304). This work was supported by the Graduate school of Post Plastic specialization of Korea Environmental Industry & Technology Institute grant funded by the Ministry of Environment, Republic of Korea. This work was supported by the Korea Institute of Energy Technology Evaluation and Planning (KETEP) and the Ministry of Trade, Industry & Energy (MOTIE) of the Republic of Korea (No. 20202020800330).

Conflict of Interest

The authors declare no conflict of interest.

Keywords: Hydrogen evolution reaction · Oxygen evolution reaction · Selenides · Urea oxidation reaction · Urine electrolysis

[1] P. Babar, A. Lokhande, V. Karade, B. Pawar, M. G. Gang, S. Pawar, J. H. Kim, *ACS Sustainable Chem. Eng.* **2019**, *7*, 10035–10043.
[2] L. Chen, J. Shi, *J. Mater. Chem. A* **2018**, *6*, 13538–13548.
[3] B. You, X. Liu, N. Jiang, Y. Sun, *J. Am. Chem. Soc.* **2016**, *138*, 13639–13646.
[4] D. Liu, T. Liu, L. Zhang, F. Qu, G. Du, A. M. Asiri, X. Sun, *J. Mater. Chem. A* **2017**, *5*, 3208–3213.
[5] V. Vedharathinam, G. G. Botte, *Electrochim. Acta* **2012**, *81*, 292–300.
[6] V. Vedharathinam, G. G. Botte, *Electrochim. Acta* **2013**, *108*, 660–665.
[7] L. Zhang, L. Wang, H. Lin, Y. Liu, J. Ye, Y. Wen, A. Chen, L. Wang, F. Ni, Z. Zhou, S. Sun, Y. Li, B. Zhang, H. Peng, *Angew. Chem. Int. Ed.* **2019**, *58*, 16820–16825; *Angew. Chem.* **2019**, *131*, 16976–16981.
[8] R. P. Forslund, J. T. Mefford, W. G. Hardin, C. T. Alexander, K. P. Johnston, K. J. Stevenson, *ACS Catal.* **2016**, *6*, 5044–5051.
[9] X. Zheng, Y. Zhang, H. Liu, D. Fu, J. Chen, J. Wang, C. Zhong, Y. Deng, X. Han, W. Hu, *Small* **2018**, *14*, 1–10.
[10] Z. Liu, C. Zhang, H. Liu, L. Feng, *Appl. Catal. B* **2020**, *276*, DOI 10.1016/j.apcatb.2020.119165.
[11] F. Guo, K. Ye, M. Du, X. Huang, K. Cheng, G. Wang, D. Cao, *Electrochim. Acta* **2016**, *210*, 474–482.
[12] X. Shi, J. Key, S. Ji, V. Linkov, F. Liu, H. Wang, H. Gai, R. Wang, *Small* **2019**, *15*, 1–10.
[13] Z. Zou, X. Wang, J. Huang, Z. Wu, F. Gao, *J. Mater. Chem. A* **2019**, *7*, 2233–2241.
[14] S. Dutta, A. Indra, Y. Feng, T. Song, U. Paik, *ACS Appl. Mater. Interfaces* **2017**, *9*, 33766–33774.
[15] H. Yang, Y. Huang, W. Y. Teoh, L. Jiang, W. Chen, L. Zhang, J. Yan, *Electrochim. Acta* **2020**, *349*, 136336.
[16] G. Wang, W. Chen, G. Chen, J. Huang, C. Song, D. Chen, Y. Du, C. Li, K. K. Ostrikov, *Nano Energy* **2020**, *71*, 104637.
[17] N. Chen, Y. Du, G. Zhang, W. Lu, F. Cao, *Nano Energy* **2021**, *81*, 105605.
[18] J. Yu, G. Cheng, W. Luo, *Nano Res.* **2018**, *11*, 2149–2158.
[19] A. Sivanantham, S. Shanmugam, *Appl. Catal. B* **2017**, *203*, 485–493.
[20] S. Anantharaj, E. Subhashini, K. C. Swaathini, T. S. Amarnath, S. Chatterjee, K. Karthick, S. Kundu, *Appl. Surf. Sci.* **2019**, *487*, 1152–1158.
[21] X. Xu, F. Song, X. Hu, *Nat. Commun.* **2016**, *7*, 1–7.
[22] B. Z. Desalegn, H. S. Jadhav, J. G. Seo, *Sustain. Energy Fuels* **2020**, *4*, 1863–1874.
[23] Y. Chen, J. Zhang, P. Guo, H. Liu, Z. Wang, M. Liu, T. Zhang, S. Wang, Y. Zhou, X. Lu, J. Zhang, *ACS Appl. Mater. Interfaces* **2018**, *10*, 27787–27794.
[24] N. Chen, Y.-X. Du, G. Zhang, W.-T. Lu, F.-F. Cao, *Nano Energy* **2021**, *81*, 105605.
[25] C. Tang, Z. Pu, Q. Liu, A. M. Asiri, X. Sun, Y. Luo, Y. He, *ChemElectroChem* **2015**, *2*, 1903–1907.
[26] Z. Yang, J. Y. Zhang, Z. Liu, Z. Li, L. Lv, X. Ao, Y. Tian, Y. Zhang, J. Jiang, C. Wang, *ACS Appl. Mater. Interfaces* **2017**, *9*, 40351–40359.
[27] J. Du, A. Yu, Z. Zou, C. Xu, *Inorg. Chem. Front.* **2018**, *5*, 814–818.
[28] Z. Wang, J. Li, X. Tian, X. Wang, Y. Yu, K. A. Owusu, L. He, L. Mai, *ACS Appl. Mater. Interfaces* **2016**, *8*, 19386–19392.
[29] Y. Huang, Y. E. Miao, J. Fu, S. Mo, C. Wei, T. Liu, *J. Mater. Chem. A* **2015**, *3*, 16263–16271.
[30] S. Ng, M. Krbal, R. Zazpe, J. Prikryl, J. Charvot, F. Dvořák, L. Strizik, S. Slang, H. Sopha, Y. Kosto, V. Matolin, F. K. Yam, F. Bures, J. M. Macak, *Adv. Mater. Interfaces* **2018**, *5*, 1–8.
[31] P. D. Tran, T. V. Tran, M. Orio, S. Torelli, Q. D. Truong, K. Nayuki, Y. Sasaki, S. Y. Chiam, R. Yi, I. Honma, J. Barber, V. Artero, *Nat. Mater.* **2016**, *15*, 640–646.
[32] J. Zhang, Y. Hu, D. Liu, Y. Yu, B. Zhang, *Adv. Sci.* **2017**, *4*, 1–7.
[33] H. Ren, Y. Pan, C. C. Sorrell, H. Du, *J. Mater. Chem. A* **2020**, *8*, 3154–3159.
[34] B. You, Y. Zhang, Y. Jiao, K. Davey, S. Z. Qiao, *Angew. Chem.* **2019**, *131*, 11922–11926; *Angew. Chem. Int. Ed.* **2019**, *58*, 11796–11800.
[35] D. Voiry, M. Chhowalla, Y. Gogotsi, N. A. Kotov, Y. Li, R. M. Penner, R. E. Schaak, P. S. Weiss, *ACS Nano* **2018**, *12*, 9635–9638.

© 2021 Wiley-VCH GmbH

18673899, 2022, 1, Downloaded from https://chemistry-europe.onlinelibrary.wiley.com/doi/10.1002/cctc.202100969 by Hanyang University Library, Wiley Online Library on [19/02/2023]. See the Terms and Conditions (https://onlinelibrary.wiley.com/terms-and-conditions) on Wiley Online Library for rules of use; OA articles are governed by the applicable Creative Commons License

[36] S. R. Kadam, A. N. Enyashin, L. Houben, R. Bar-Ziv, M. Bar-Sadan, *J. Mater. Chem. A* **2020**, *8*, 1403–1416.
[37] B. Zhang, J. Liu, J. Wang, Y. Ruan, X. Ji, K. Xu, C. Chen, H. Wan, L. Miao, J. Jiang, *Nano Energy* **2017**, *37*, 74–80.
[38] C. Hu, L. Zhang, Z. J. Zhao, A. Li, X. Chang, J. Gong, *Adv. Mater.* **2018**, *30*, 1–8.
[39] J. Xin, H. Tan, Z. Liu, L. Zhao, J. Xie, Y. Sang, W. Zhou, A. Wang, H. Liu, J. J. Wang, *Nanoscale* **2019**, *11*, 3240–3247.
[40] J. Xie, J. Xin, R. Wang, X. Zhang, F. Lei, H. Qu, P. Hao, G. Cui, B. Tang, Y. Xie, *Nano Energy* **2018**, *53*, 74–82.
[41] S. Lee, K. Banjac, M. Lingenfelder, X. Hu, *Angew. Chem.* **2019**, *131*, 10401–10405; *Angew. Chem. Int. Ed.* **2019**, *58*, 10295–10299.
[42] D. Singh, Analysis of Urea Electrolysis for Generation of Hydrogen, **2009**.
[43] K. Lemoine, J. Lhoste, A. Hémon-Ribaud, N. Heidary, V. Maisonneuve, A. Guiet, N. Kornienko, *Chem. Sci.* **2019**, *10*, 9209–9218.
[44] W. Zhu, Z. Yue, W. Zhang, N. Hu, Z. Luo, M. Ren, Z. Xu, Z. Wei, Y. Suo, J. Wang, *J. Mater. Chem. A* **2018**, *6*, 4346–4353.
[45] R. L. Doyle, M. E. G. Lyons, *Phys. Chem. Chem. Phys.* **2013**, *15*, 5224–5237.
[46] G. Wang, K. Ye, J. Shao, Y. Zhang, K. Zhu, K. Cheng, J. Yan, G. Wang, D. Cao, *Int. J. Hydrogen Energy* **2018**, *43*, 9316–9325.
[47] Z. Qiu, Y. Ma, T. Edvinsson, *Nano Energy* **2019**, *66*, 104118.
[48] Z. Wang, P. Guo, M. Liu, C. Guo, H. Liu, S. Wei, J. Zhang, X. Lu, *ACS Appl. Mater. Interfaces* **2019**, *2*, 3363–3372.
[49] R. Suresh, K. Giribabu, R. Manigandan, A. Stephen, V. Narayanan, *RSC Adv.* **2014**, *4*, 17146–17155.
[50] J. Lu, Y. Xiong, C. Liao, F. Ye, *Anal. Methods* **2015**, *7*, 9894–9899.
[51] S. K. Ponnaiah, P. Periakaruppan, B. Vellaichamy, *J. Phys. Chem. B* **2018**, *122*, 3037–3046.
[52] M. Akram, M. N. Asghar, M. Saleem Khan, S. Shahid, H. M. Abdur Rahman, I. Nadeem, *Biosci. Biotechnol. Biochem.* **2020**, *84*, 1–8.

Manuscript received: July 2, 2021
Revised manuscript received: August 28, 2021
Accepted manuscript online: September 7, 2021
Version of record online: September 20, 2021

© 2021 Wiley-VCH GmbH

18673899, 2022, 1, Downloaded from https://chemistry-europe.onlinelibrary.wiley.com/doi/10.1002/cctc.202100969 by Hanyang University Library, Wiley Online Library on [19/02/2023]. See the Terms and Conditions (https://onlinelibrary.wiley.com/terms-and-conditions) on Wiley Online Library for rules of use; OA articles are governed by the applicable Creative Commons License